

# Fano Resonance Based on End-Coupled Cascaded-Ring MIM Waveguides Structure

Kunhua Wen<sup>1</sup> · Yihua Hu<sup>1</sup> · Li Chen<sup>1</sup> · Jinyun Zhou<sup>1</sup> · Miao He<sup>1</sup> · Liang Lei<sup>1</sup> · Ziming Meng<sup>1</sup> · Yanjie Wu<sup>1</sup> · Jianfeng Li<sup>1</sup>

Received: 1 August 2016 / Accepted: 25 November 2016 / Published online: 5 December 2016  
© Springer Science+Business Media New York 2016

**Abstract** Though adding a groove to a plasmonic end-coupled perfect ring (PR) resonator, two additional resonance modes, which can be controlled by the length of the groove, will arise in this proposed ring-groove (RG) joint metal-insulator-metal (MIM) waveguide. By further cascading, the PR resonator and the RG joint resonator, single and dual Fano resonances with asymmetric line shapes are obtained due to the interference effects between the dark modes and the bright modes. High figure of merit and high refractive-index sensitivity are achieved, and thus this structure is suitable for the biochemistry sensing area. Interestingly, normal and abnormal dispersions are also investigated for the Fano peaks and dips, respectively. The performances of the proposed structure are investigated by using the finite-difference time-domain method.

**Keywords** Plasmonic · Resonator · Metal-insulator-metal waveguide · Fano resonance

## Introduction

Recently, plasmonic metal-insulator-metal (MIM) waveguides [1–5], which are considered as one of the most promising ways for nano-integrated photonic circuits, have attracted a lot of interest in the all-optical signal processing area. Various outstanding characteristics for MIM waveguides

are successively explored, such as wavelength selection, power splitting, Fano resonance, electromagnetically induced transparency (EIT), and so on [6–17]. Especially for the Fano resonance, it was firstly achieved in the auto-ionizing states of atoms [18]. Unlike the Lorenz symmetric line shape of Fabry–Pérot (FP) resonance, Fano resonance is with the asymmetric sharp transmission/reflection spectrum, which shows a great potential in the optical signal processing and sensing areas due to the unique advantages of high figure of merit (FOM) and high sensitivity. However, hard operation conditions limit its development, and then alternative plasmonic induced Fano effects are demonstrated in various MIM waveguide structures [19–21]. Owing to the strong destructive interference between the bright and dark modes, which are generated from the directly and indirectly coupled resonators, respectively, the Fano phenomenon have been observed in the dual-disk, dual-ring, dual-slot-cavity, gear-shaped resonators [22–26]. In view of the demands of nanosensor, the FOM was further improved by employing an MIM T-shaped resonator [27]. Dual Fano resonances, which could provide two independent channels, were also investigated by using slot cavity-groove cascaded MIM structures [28, 29].

In this paper, an end-coupled ring-groove (RG) joint MIM waveguide structure is proposed. Unlike the perfect ring (PR) structures that are regarded as the FP resonator, two additional resonance modes are generated by adding a groove in the PR. According to the interference effect, single and dual Fano resonances can also be achieved by cascading the PR and RG joint resonators, which can provide the dark and bright modes, respectively. High FOM and high refractive-index sensitivity, which are suitable for the biochemistry sensing, are obtained. The group time delay for the peaks and dips are also investigated. The performances are investigated by using the finite-difference time-domain (FDTD) method.

✉ Kunhua Wen  
khwen@gdut.edu.cn

<sup>1</sup> School of Physics and Optoelectronic Engineering, Guangdong University of Technology, Guangzhou, Guangdong 510006, China

## Theory and Simulations

The end-coupled PR structure is shown in Fig. 1a. A PR resonator, whose inner and outer radius are defined as  $r$  and  $R$ , respectively, locates between the input and output MIM waveguides with the coupling distances  $s_1$ ,  $s_2$ . The widths of the output and input waveguides are the same as  $D$ . The metal and insulator are defined as silver and air for the MIM waveguide, respectively, and the optical constants are obtained from the experiment [30]. Since the PR is regarded as an FP resonator, the resonance condition of the PR can be approximately given by

$$\lambda_m = 2\text{Re}(n_{\text{eff}})L_{\text{eff}}/m, \quad m = 1, 2, 3, \dots, \quad (1)$$

where  $m$  stands for the order of the resonance mode,  $L_{\text{eff}} = \pi(r+R)/2$  is the effective resonance length,  $\text{Re}(n_{\text{eff}})$  is the real part of the effective refractive index  $n_{\text{eff}}$  obtained from the dispersion Eqs. [31]:  $\varepsilon_i k_{z2} + \varepsilon_m k_{z1} \coth(-ik_{z1}D/2) = 0$ ,  $D$  is the width of the waveguide,  $k_{z1,2} = \sqrt{\varepsilon_{i,m}k_0^2 - (k_0 n_{\text{eff}})^2}$  is the transverse propagation constant in the insulator or metal,  $k_0 = 2\pi/\lambda$  is the free space wave-vector,  $\varepsilon_i$  and  $\varepsilon_m$  are the dielectric constants of the dielectric medium and the metal, respectively. During the FDTD simulations, the following parameters are the same all through the paper: the widths of the input and output waveguides are  $D = 50\text{nm}$ , and the inner and outer radius are defined as  $r = 170\text{nm}$ , and  $R = 220\text{nm}$ , respectively.

In Fig. 1b, the coupling distances in the left and right sides are  $s_1 = 5\text{nm}$ , and  $s_2 = 10\text{nm}$ , respectively. The transmission spectrum for the PR resonator shows that the 1st and 2nd order resonance modes with high transmittances are achieved at the wavelengths of 1771.1 and 891.6 nm, respectively. In Fig. 1c, the coupling distances are defined as  $s_1 = 5\text{nm}$ , and  $s_2 = 10\text{nm}$  (black line),  $s_1 = 10\text{nm}$ , and  $s_2 = 10\text{nm}$  (red line),  $s_1 = 10\text{nm}$ , and  $s_2 = 15\text{nm}$  (blue line), and other parameters are the same as that in Fig. 1b. Actually, the center wavelength will have a slight shift and the transmittance will be affected by increasing the coupling distance. However, it can be seen that there are always two resonance modes, i.e., the 1st-order mode and the 2nd-order mode. Therefore, we can still use Eq. (1) to

approximately estimate the resonance wavelengths. This kind of structure can serve as an on-chip optical filter, which has been widely demonstrated. The corresponding magnetic field distributions at the peak wavelengths are also shown in Fig. 1b. Obviously, there is a node for the 1st mode at the top of the PR resonator, while an antinode for the 2nd mode locates near the top. In this case, when a groove is placed at this position, as shown in Fig. 2a, SPPs for the 2nd mode will be captured into the groove but the 1st mode will not be affected, and therefore, all the following analyses refer to the 2nd mode. Specifically, a groove, whose width and length are defined as  $W$  and  $L$ , respectively, is placed at the inner top of the PR structure, while other parameters of the PR are the same as that in Fig. 1a. Then, destructive interference will occur near the output MIM waveguide, when the phase difference  $\Delta\theta$  between the upper circle and the below circle of RG joint structure satisfies the condition:

$$\Delta\theta = 2kL + \varphi = (2m + 1)\pi \quad m = 0, 1, 2, \dots \quad (2)$$

where  $k = 2\pi\text{Re}(n_{\text{eff}})/\lambda$  is the wave-vector inside the waveguide,  $L$  is the length of the groove, and  $\varphi$  is the phase delay caused by the reflection at the end of the groove. In this case, a band gap with an abnormal dispersion will arise at the wavelength of the former transmission peak.

By setting  $L = 110\text{nm}$  and  $W = 30\text{nm}$ , the transmission spectrum is shown in Fig. 2b with a red-solid line. For easily comparison, the transmission spectrum for the PR resonator is also plotted in Fig. 2b with black-dotted line. Obviously, an absorbed window is obtained, since the previous peak at 891.6 nm (i.e., the 2nd mode of the PR resonator) is replaced by a forbidden band after adding the groove to the PR structure. Meanwhile, the 1st mode keeps no changes as the analysis above. Besides, two new transmission peaks, which are called as bight modes 1 and 2 (i.e., BM1 and BM2), are achieved with transmittances of  $\sim 0.6$  at the wavelengths of 775.3 and 1038.4 nm, respectively. Figure 2c–d shows the magnetic field distributions of the transmission peaks and the forbidden band, which are marked with “A, B, C” in Fig. 2b. Obviously, SPPs for the transmission peaks can pass through the output waveguide in Figs. 2c and e, while the ones for the band-gap in Fig. 2d are stopped by the RG structure.

**Fig. 1** (a) Scheme diagram of the end-coupled PR structure, (b) transmission spectrum and the magnetic field, and (c) transmission spectra with different coupling distances

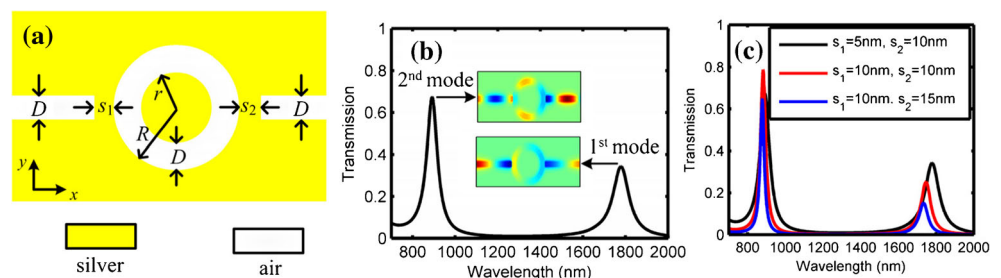
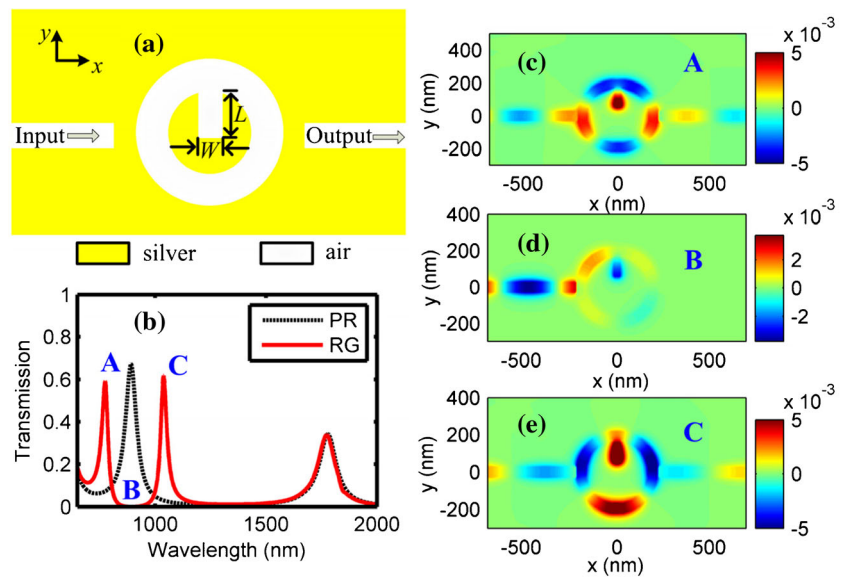


**Fig. 2** (a) Transmission spectra for the PR and RG joint structure, (b) reflection spectrum for the RG joint structure, and (c)–(e) magnetic field distributions corresponding to the wavelengths of “A, B, C” in (a)



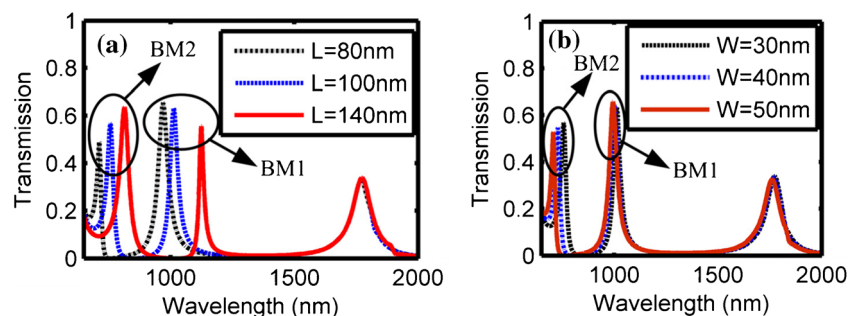
Interestingly, by comparing to the field distribution in Figs. 2c or e, reversed phase occurs at the groove in Fig. 2d. Therefore,  $\pi$  phase difference between the upper circle and the below circle is achieved, leading to the destructive interference at the right side of the ring.

According to Eq. (2), the forbidden band will be affected by the length  $L$  and the width  $W$  of the groove. In Fig. 3a, it can be found out that the absorption window and the bright modes (BM1 and BM2) at its both sides have a redshift by setting  $W = 30\text{nm}$ , and  $L = 80\text{nm}$ ,  $100\text{nm}$ , and  $140\text{nm}$ , respectively. It is investigated that the wavelength has a linear proportion relationship with  $L$ . Besides, there is always a transmission peak available at  $1771.1\text{ nm}$ , which further indicates that the transmission peak of the 1st mode will not be changed by the length of the groove. In Fig. 3b, the length of the groove is  $100\text{ nm}$  and the width of the groove is defined as  $W = 30\text{ nm}$ ,  $40\text{ nm}$ , and  $50\text{ nm}$ , respectively. In this case, both BM1 and BM2 modes have a blueshift when increasing  $W$ , since  $\text{Re}(n_{\text{eff}})$  for the groove decreases. This kind of structure can find important applications in the optical filtering area, and therefore, one can design the filtering system with a flexible wavelength manipulation by setting the parameter  $L$ .

Moreover, it can be observed that the transmission peaks (bright modes of BM1 and BM2) for the RG structure coincides with the band-gaps (dark modes) for the PR structure through getting insight into the transmission spectra in Fig. 2b. According to the mode-interference effect, we can further explore the Fano resonance by cascading the PR and RG joint structure, as shown in Fig. 4. The localized dark mode (corresponding to the discrete excited state) and the radiative bright mode (corresponding to the continuum state) can be excited by the PR and RG structures, respectively. Fano resonance will then be generated because of the interaction between the dark mode and the bright mode. Different from the Lorentzian resonance, a distinctly asymmetrical spectral profile, which has a sharp transmission peak and an ultra steep dip, is achieved for the Fano resonance.

By setting the coupling distance  $s_3 = 5\text{nm}$ ,  $L = 80\text{nm}$ ,  $110\text{nm}$ ,  $160\text{nm}$ , and keeping other parameters unchanged, the transmission spectra are shown in Fig. 5a–c based on the FDTD method. Firstly, SPPs are directly coupled into the end-coupled PR structure, which can still perform as an FP resonator. Therefore, the 1st and the 2nd resonance modes always remain at the same wavelengths of  $1771$  and  $892\text{ nm}$  from

**Fig. 3** Transmission spectra of the RG joint structure (a) with different lengths of the groove (b) with different widths of the groove



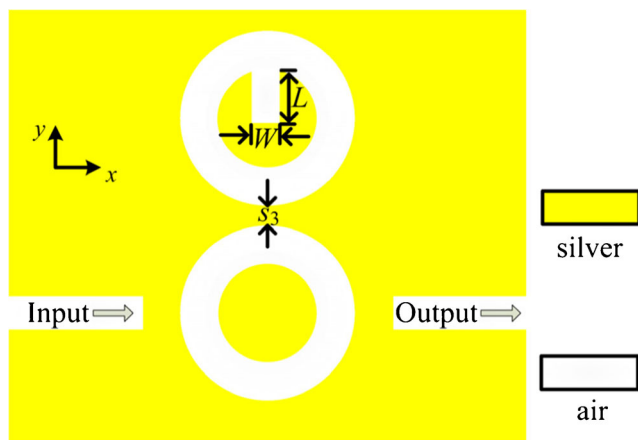


**Fig. 4** Scheme diagram of the PR-RG cascaded structure

Fig. 5a–c, respectively. The results agree well with that in Fig. 1, and it also means that the filtering function for the PR in this proposed structure still operates normally. In addition to these two symmetric transmission peaks, single or dual asymmetrical Fano peaks with asymmetric line shapes are achieved near the 2nd mode as well. The Fano resonance can be manipulated by using the length of the groove, which controls the wavelengths of the bright modes of BM1 and BM2, as illustrated in Fig. 3. Only when the frequency of the bright mode in the RG structure is approximately near the edge of the dark mode in the PR structure, the interference effect between the two modes will then occur, leading to the Fano resonance. Therefore, one sharp Fano peak with transmittance of ~0.44 is available at 975.5 nm in Fig. 5a, because only the BM1 mode interacts with the dark mode in the PR structure. The transmission dip, which reaches the minimum at 956.5 nm, arises at the left side of the peak. By increasing the length  $L = 110\text{nm}$ , dual Fano peaks at 768.0 and 1038.0 nm with transmittances of ~0.2 are obtained in

**Fig. 5** The Fano spectra in (a)–(c) with  $L = 80, 110, 160$  nm, respectively, and the  $\text{FOM}^*$  in (e)–(f) corresponding to the spectra in (a)–(c)

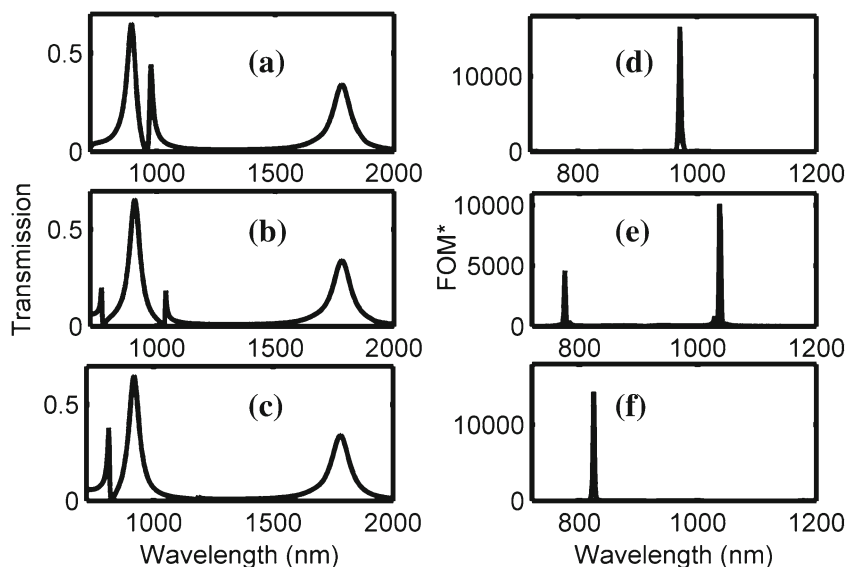


Fig. 5b as a result of the redshift of the BM1 and BM2 modes. The two Fano spectra profiles possess different line shapes as the transmission dips with the minimums at 1030.0 and 775.5 nm are distributed at the left and right sides of the peaks, respectively. By further setting the length  $L$  to be 160 nm in Fig. 5c, there is also one Fano peak with a transmittance of ~0.38 at 911.8 nm. By comparing to the spectrum in Fig. 5a, the spectral profile in Fig. 5c presents an obvious transformation after changing  $L$  in view of the distribution of the steep dip. The reversal mechanism of the asymmetric spectral profile can also be attributed to the shift of the narrow bright modes, and only the BM2 mode will interact with the broad dark mode. Therefore, one can conveniently obtain the single and dual Fano resonance peaks by designing the length of the groove, and this kind of structure can find widely applications in the sensing and optical signal processing areas.

To further evaluate the sensing performances of the proposed structures, the sensitivity  $S$  and FOM are used and expressed as [32, 33]

$$S = \frac{d\lambda}{dn(\lambda)} \tag{3}$$

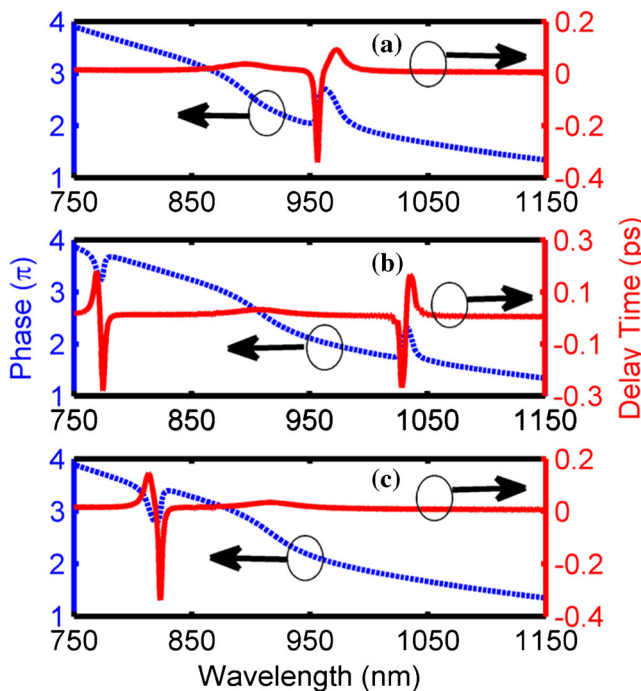
$$\text{FOM}^* = \left| \frac{dT(\lambda)/dn(\lambda)}{T(\lambda)} \right| \tag{4}$$

$$\text{FOM} = \text{Max}(\text{FOM}^*) \tag{5}$$

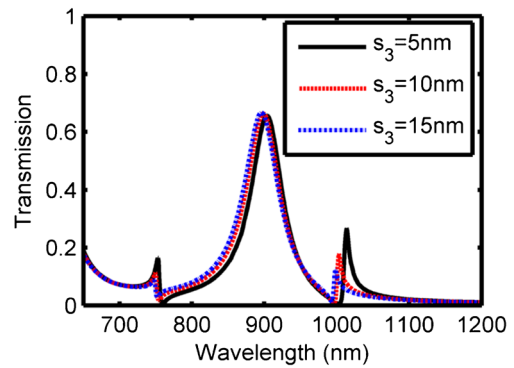
where  $T(\lambda)$  is the transmittance, and  $dT(\lambda)/dn(\lambda)$  is the transmittance variation induced by the change of a refractive index. Based on Eqs. (3) and (4), it can be predicted that an ultra-low transmittance and a sharp increase of the transmittance induced by the index changes are preferred for obtaining a high FOM. According to the spectra in Fig. 5a–c, the values of  $S$  and FOM are calculated as 960 nm/RIU and  $1.65 \times 10^4$  in

Fig. 5d, respectively; 750 nm/RIU and  $0.46 \times 10^4$  for the left Fano peak, and 1050 nm/RIU and  $1.01 \times 10^4$  for the right Fano peak in Fig. 5e, respectively; 800 nm/RIU and  $1.44 \times 10^4$  in Fig. 5f, respectively. In view of these outstanding characteristics, it is believed that the proposed structure will be preferred in the sensing area.

The dispersion  $d_p$  and the delay time  $\tau$  satisfy the conditions:  $\tau(\lambda) = -\lambda^2 d\theta/2\pi cd\lambda$  and  $d_p = d\tau/d\lambda$ , respectively. In this case, the phase responses and the delay time for the Fano resonances in Fig. 5a–c are also analyzed in Fig. 6a–c, respectively. Obviously, the phase shifts, which are plotted by using blue-dotted lines, will occur at each Fano peak and dip but with different variation tendencies. More detailed results can be distinguished from the delay time in Fig. 6 with red-solid lines. Negative and positive delay time is achieved for the Fano dips and peaks, respectively. Specifically, the results are  $-0.34$  and  $0.09$  ps in Fig. 6a, respectively;  $-0.28$  and  $0.18$  ps for the left Fano resonance, and  $-0.27$  and  $0.17$  ps for the right resonance in Fig. 6b, respectively;  $-0.34$  and  $0.15$  ps in Fig. 6c, respectively. In addition to the sensing applications, one can also easily obtain the normal and abnormal dispersion by using the Fano peaks or the dips in this proposed structure, which is therefore suitable for the optical switching and optical storage areas. As for the 2nd mode at 893 nm, the variation of the phase curve is quite smooth, and therefore, almost no delay time will arise within the wavelength of the 2nd mode. In this case, this transmission peak can be used as a wavelength filter without a dispersion effect.



**Fig. 6** The variations of the phase response and the delay time with respect to the wavelength



**Fig. 7** Fano spectra with different coupling distance  $s_3$

Finally, the influence of the coupling distance  $s_3$  on the Fano resonance is discussed. In Fig. 7, the parameters are the same as that used in Fig. 5a, and the coupling distance  $s_3$  is defined as 5, 10, and 15 nm, respectively. Obviously, the transmittances of both Fano peaks decrease when increasing  $s_3$  and their wavelengths have a slight blueshift as well. It can be concluded that a small coupling distance leads to a high-quality Fano resonance but a difficult manufacture process. Therefore, one should find a balance between the performance and the manufacture cost.

### Summary

In summary, due to the interference effect after adding a groove to the PR structure, an absorption window and two new transmission peaks were induced. By taking advantage of the cascaded RG/PR structures which supported the bright and dark modes, respectively, single or dual Fano resonances have been obtained. The asymmetric line shapes, which could be manipulated by changing the length of the groove, were also achieved owing to the mode interactions. The device could serve as an on-chip nano sensor due to the highest sensitivity and FOM as 1050 nm/RIU and  $1.65 \times 10^4$ , respectively.

**Acknowledgements** The work is supported by the National Natural Science Foundation of China under Grants No. 61405039 and No. 61475037, Science and Technology Planning Projects of Guangdong Province, China under Grant No. 2016A020223013, the Natural Science Foundation of Guangdong Province, China, under Grant No. 2014A030310300, the State Key Lab of Optical Technologies for Micro-Engineering and Nano-Fabrication of China, the Foundation for Distinguished Young Talents in Higher Education of Guangdong, China, under Grant No. 2014KQNCX066, Research Fund for the Doctoral Program of Higher Education of China under Grant No. 20134407110008, Guangzhou Science and Technology Project of Guangdong Province, China under Grant No. 2016201604030027, Research Project of Guangdong Province under Grant No. 2013B090500035, and the Science and Technology Program of Guangzhou under Grant No. 2014 J4100202.

**Compliance with Ethical Standards** The authors declare that they have no conflict of interest.

## References

- Song G, Yu L, Wu C, Duan G, Wang L, Xiao J (2013) Polarization splitter with optical bistability in metal gap waveguide nanocavities. *Plasmonics* 8(2):943–947
- Liu Y, Zhou F, Yao B, Cao J, Mao Q (2013) High-extinction-ratio and low-insertion-loss plasmonic filter with coherent coupled nanocavity array in a MIM waveguide. *Plasmonics* 8(2):1035–1041
- Chen Z, Song XK, Duan GY, Wang LL, Yu L (2015) Multiple Fano resonances control in MIM side-coupled cavities systems. *IEEE Photon J* 7(3):2701009
- Wen KH, Hu YH, Chen L, Zhou JY, He M, Lei L, Meng ZM (2015) Multiple plasmon-induced transparency responses in a subwavelength inclined ring resonators system. *IEEE Photon J* 7(6):1–7
- Wen KH, Hu YH, Chen L, Zhou JY, Lei L, Meng ZM (2016) Plasmonic bidirectional/unidirectional wavelength splitter based on metal-dielectric-metal waveguides. *Plasmonics* 11(1):71–77
- Nikolajsen T, Leosson K, Bozhevolnyi SI (2004) Surface Plasmon polariton based modulators and switches operating at telecom wavelengths. *Appl Phys Lett* 85(24):5833–5835
- Lu H, Liu XM, Wang L, Gong Y, Mao D (2011) Ultrafast all-optical switching in nanoplasmonic waveguide with Kerr nonlinear resonator. *Opt Express* 19(4):2910–2915
- Wurtz GA, Pollard R, Zayats AV (2006) Optical bistability in nonlinear surface-plasmon polaritonic crystals. *Phys Rev Lett* 97(5):057402
- Randhawa S, González MU, Renger J, Enoch S, Quidant R (2010) Design and properties of dielectric surface plasmon Bragg mirrors. *Opt Express* 18(14):14496–14510
- Bozhevolnyi SI, Volkov VS, Devaux E, Laluet JY, Ebbesen TW (2006) Channel plasmon subwavelength waveguide components including interferometers and ring resonators. *Nature* 440(7083):508–511
- Enoch S, Quidant R, Badenes G (2004) Optical sensing based on plasmon coupling in nanoparticle arrays. *Opt Express* 12(15):3422–3427
- Park J, Kim H, Lee B (2008) High order plasmonic Bragg reflection in the metal-insulator-metal waveguide Bragg grating. *Opt Express* 16(1):413–425
- Hu FF, Yi HX, Zhou ZP (2011) Wavelength demultiplexing structure based on arrayed plasmonic slot cavities. *Opt Lett* 36(8):1500–1502
- Ma FS, Lee C (2013) Optical nanofilters based on meta-atom side-coupled plasmonics metal-insulator-metal waveguides. *J Lightwave Technol* 31(17):2876–2880
- Pu MB, Hu CG, Huang C, Wang CT, Zhao ZY, Wang YQ, Luo XG (2013) Investigation of Fano resonance in planar metamaterial with perturbed periodicity. *Opt Express* 21(1):992–1001
- Pu MB, Li X, Ma XL, Wang YQ, Zhao ZY, Wang CT, Hu CG, Gao P, Huang C, Ren HR, Li XP, Qin F, Yang J, Gu M, Hong MH, Luo XG (2015) Catenary optics for achromatic generation of perfect optical angular momentum. *Sci Adv* 1(9):e1500396
- Luo X, Zou X, Li X, Zhou Z, Pan W, Yan L, Wen KH (2013) High-uniformity multichannel plasmonic filter using linearly lengthened insulators in metal-insulator-metal waveguide. *Opt Lett* 38(9):1585–1587
- Luk'yanchuk B, Zheludev N, Maier S, Halas N, Nordlander P, Giessen H, Chong C (2010) The Fano resonance in plasmonic nanostructures and metamaterials. *Nat Mater* 9(9):707–715
- Chen J, Li Z, Zou Y, Deng Z, Xiao J, Gong Q (2013) Coupled-resonator-induced Fano resonances for plasmonic sensing with ultra-high figure of merits. *Plasmonics* 8(4):1627–1631
- Piao X, Yu S, Koo S, Lee K, Park N (2011) Fano-type spectral asymmetry and its control for plasmonic metal-insulator-metal stub structures. *Opt Express* 19(11):10907–10912
- Qi J, Chen Z, Chen J, Li Y, Qiang W, Xu J, Sun Q (2014) Independently tunable double Fano resonances in asymmetric MIM waveguide structure. *Opt Express* 22(12):14688–14695
- Paul S, Bera M, Ray M (2015) Parametric analysis of spectral Fano lineshape for plasmonic waveguide-coupled dual nanoresonator. *J Lightwave Technol* 33(13):2824–2830
- Li BX, Li HJ, Zeng LL, Zhan SP, He ZH, Chen ZQ, Xu H (2016) Sensing application in Fano resonance with T-shape structure. *J Lightwave Technol* 34(14):3342–3347
- Zhan S, Peng Y, He Z, Li B, Chen Z, Xu H, Li H (2016) Tunable nanoplasmonic sensor based on the asymmetric degree of Fano resonance in MDM waveguide. *Sci Rep* 6:22428
- Fan C, Shi F, Wu H, Chen Y (2015) Tunable all-optical plasmonic diode based on Fano resonance in nonlinear waveguide coupled with cavities. *Opt Lett* 40(11):2449–2452
- Zhang ZD, Wang HY, Zhang ZY (2013) Fano resonance in a gear-shaped nanocavity of the metal-insulator-metal waveguide. *Plasmonics* 8(2):797–801
- Wen K, Hu Y, Chen L, Zhou J, Lei L, Guo Z (2015) Fano resonance with ultra-high figure of merits based on plasmonic metal-insulator-metal waveguide. *Plasmonics* 10(1):27–32
- Chen Z, Yu L (2014) Multiple Fano resonances based on different waveguide modes in a symmetry breaking plasmonic system. *IEEE Photon J* 6(6):1–8
- Wen KH, Hu YH, Chen L, Zhou JY, Lei L, Meng ZM (2016) Single/dual Fano resonance based on plasmonic metal-dielectric-metal waveguide. *Plasmonics* 11(1):315–321
- Johnson PB, Christy RW (1972) Optical constants of the noble metals. *Phys Rev B* 6:4370–4379
- Dionne JA, Sweatlock LA, Atwater HA (2006) Plasmon slot waveguides: towards chip-scale propagation with subwavelength-scale localization. *Phys Rev B* 73:035407
- Becker J, Trügler A, Jakab A, Hohenester U, Sönnichsen C (2010) The optimal aspect ratio of gold nanorods for plasmonic bio-sensing. *Plasmonics* 5(2):161–167
- Lu H, Liu X, Mao D, Wang G (2012) Plasmonic nanosensor based on Fano resonance in waveguide-coupled resonators. *Opt Lett* 37(18):3780–3782